China Ocean Eng., 2023, Vol. 37, No. 4, P. 685–697
DOI: https://doi.org/10.1007/s13344-023-0057-8, ISSN 0890-5487
http://www.chinaoceanengin.cn/ E-mail: coe@nhri.cn

Influences of Floater Motion on Gap Resonance Triggered by Focused Wave Groups

GAO Jun-liang[a, b, c], LYU Jing[a], ZHANG Jian[a, *], ZANG Jun[d]

[a] School of Naval Architecture and Ocean Engineering, Jiangsu University of Science and Technology, Zhenjiang 212100, China

[b] Key Laboratory of Port, Waterway and Sedimentation Engineering of MOT, Nanjing Hydraulic Research Institute, Nanjing 210029, China

[c] Key Laboratory of Water Security Guarantee in Guangdong-Hong Kong-Marco Greater Bay Area of Ministry of Water Resources, Guangzhou 510611, China

[d] Centre for Infrastructure, Geotechnical and Water Engineering (IGWE), Department of Architecture and Civil Engineering, University of Bath, BA2 7AY, UK

Received January 21, 2023; revised April 14, 2023; accepted June 6, 2023

Abstract

The current study investigates the hydrodynamic characteristics of gap resonance within a narrow gap formed by two adjacent boxes subjected to incident focused transient wave groups. A two-dimensional (2D) numerical wave tank based on the OpenFOAM package is utilized for this purpose. The weather-side box is fixed while the lee-side box is allowed to heave freely under wave actions. The effects of the focused wave amplitude and spectral peak period on the wave amplification within the gap, motion of the lee-side box, and wave forces (including horizontal and vertical wave forces) acting on each box are systematically examined. For comparison, another structural layout consisting of two fixed boxes is also considered. The results reveal that the release of the heave degree of freedom (DoF) of the lee-side box results in remarkably distinct resonance features. In the heave-box system, both its fluid resonant period and the period corresponding to the maximum heave displacement of the lee-side box are significantly larger (i.e., 1.6−1.7 times) than the fluid resonant period of the fixed-box system. However, the wave amplification factor inside the gap in the heave-box system is significantly lower than that in the fixed-box one. Both the variations of the maximum horizontal and vertical wave forces with the spectral peak period and their magnitudes are also significantly different between the two structural systems.

Key words: gap resonance, focused waves, wave amplification, wave forces, OpenFOAM

Citation: Gao, J.L., Lyu, J., Zhang, J., Zang, J., 2023. Influences of floater motion on gap resonance triggered by focused wave groups. China Ocean Eng., 37(4): 685–697, doi: https://doi.org/10.1007/s13344-023-0057-8

1 Introduction

In the past few decades, the development and exploitation of offshore oil and gas resources have experienced tremendous growth. Operations involving multiple floaters deployed in close proximity and side by side, such as the Floating Liquefied Natural Gas (FLNG) production system and Liquefied Natural Gas Carrier (LNGC), have become more prevalent (Song et al., 2022; Zhao et al., 2018). However, a fluid resonance phenomenon characterized by strong fluid motions, known as “gap resonance”, may occur inside the narrow gap between two floaters (He et al., 2021a, 2021b; Ning et al., 2018). It can cause a significant increase in both hydrodynamic forces and floater motion, ultimately affecting the safety of offshore operations (Jing et al., 2022; Liang et al., 2022). In fact, in the fields of coastal and offshore engineering, there are other similar resonant phenomena of water bodies, such as liquid sloshing restricted by a partially-filled container (Jiang et al., 2022; Liang et al., 2020) and harbor resonance restricted by bays or harbors (Gao et al., 2023a, 2023c).

During the initial stages of research on gap resonance, numerical simulations and theoretical analyses were primarily

Foundation item: This research is financially supported by the National Natural Science Foundation of China (Grant No. 51911530205), the Natural Science Foundation of Jiangsu Province (Grant No. BK20201455), the Guangdong Basic and Applied Basic Research Foundation (Grant No. 2023A1515010890), the Key Laboratory of Port, Waterway and Sedimentation Engineering of MOT (Grant No. YK222001-2), the Open Research Fund of Key Laboratory of Water Security Guarantee in Guangdong-Hong Kong-Marco Greater Bay Area of Ministry of Water Resources (Grant No. WSGBA-KJ202309), and the Qing Lan Project of Jiangsu Universities. The authors also thank the Royal Society (Grant No. IEC\NSFC\181321) for providing partial support for this work.

*Corresponding author. E-mail: justzj@126.com

based on the classical potential flow theory. However, the theory has been shown to notably overpredict both the wave elevation inside the narrow gap and the wave forces acting on floaters due to the neglect of the viscous effect of real fluids (e.g., Miao et al., 2001; Molin, 2001; Zhu et al., 2008). To address this drawback, scholars proposed various methodologies to incorporate artificial viscosity into the classical potential flow theory, such as adding damping at the free water surface (e.g., Ning et al., 2015) or at a submerged surface (e.g., Liang et al., 2021; Wang et al., 2022). To validate the accuracy of existing analytical and numerical models and to gain a better understanding of related hydrodynamic characteristics, laboratory experiments were conducted in 2D wave tanks (e.g. Kristiansen and Faltinsen, 2010; Saitoh et al., 2006; Tan et al., 2014) and 3D wave basins (e.g., Feng et al., 2020; Li et al., 2016; Perić and Swan, 2015; Zhao et al., 2017) to simulate the gap resonance phenomenon.

Over the past decade, the use of Computational Fluid Dynamics (CFD) models in investigating gap resonance has become increasingly common, owing to the rapid development of computer science. It includes two categories of CFD models. The first and most commonly used category is mesh-based numerical models, such as the open-sourced package OpenFOAM (e.g., Gao et al., 2019a, 2020b; He et al., 2021c; Liu et al., 2022) and the commercial software Star-CCM+ (e.g., Ding et al., 2022a, 2022b). The second category is mesh-free numerical models, such as the Smoothed Particles Hydrodynamics (SPH) model (e.g., Meringolo et al., 2018) and the Improved Meshless Local Petrov-Galerkin method based on Rankine source function (IMLPG_R) (e.g., Vineesh and Sriram, 2021). All these CFD models have been found to be effective in reproducing existing laboratory experiments because of their proper consideration of fluid viscosity.

Despite numerous studies on gap resonance, most have only considered the steady-state resonance induced by incident regular waves (e.g., Cong et al., 2022; Gao et al., 2023b; Jiang et al., 2019, 2020; Li, 2019; Liang et al., 2021; Lu et al., 2020; Perić and Swan, 2015; Song et al., 2021; Tan et al., 2020; Wang and Zou, 2007; Zou et al., 2023). However, under real sea conditions, waves are often stochastic and transient (Fan et al., 2023; Fu et al., 2021; He et al., 2023), making it challenging for gap resonance to reach steady state in many situations. For this reason, a few scholars have investigated the transient fluid resonance in narrow gaps induced by focused wave groups (e.g., Eatock Taylor et al., 2008; Gao et al., 2020a; Vineesh and Sriram, 2021; Zhao et al., 2017).

To the best of the authors' knowledge, previous investigations on the transient gap resonance induced by incident focused waves have primarily assumed that all floaters forming the narrow gap are fixed. However, in many practical applications, some floaters (such as LNGC) are allowed to move to a certain extent. This article continues to focus on the transient gap resonance induced by focused wave groups, in which the lee-side floater is allowed to heave freely under wave actions. For comparison, the transient gap resonance formed between two fixed floaters is also considered. This study aims to investigate the effect of floater motion on the hydrodynamic characteristics of gap resonance induced by focused wave groups. Specifically, this paper seeks to answer the following three questions:

(1) What is the spectral peak period of the incident wave groups at which the lee-side floater can reach its maximum heave displacement?

(2) How does the floater motion affect the changing trends of fluid resonant period and wave amplification factor with respect to the incident wave period and focused wave amplitude?

(3) How do the variations of wave forces (including horizontal and vertical forces) with respect to the incident wave period and focused wave amplitude differ due to the floater motion?

The article continues with the details of the numerical model and the generation principles of focused wave groups in Section 2. The numerical wave tank utilized is introduced in Section 3. These are followed by the simulation results and discussion in Section 4. The article ends in Section 5 with some concluding remarks.

2 Numerical model and generation principles of focused wave groups

2.1 Description of the numerical model

To accurately consider the energy dissipation near marine structures caused by fluid viscosity during gap resonance, a viscous flow solver is necessary. In the current study, a viscous numerical wave tank is established based on the open-sourced CFD software package, OpenFOAM (version 3.0.1). The built-in two-phase flow solver "interFoam", combined with the toolbox "waves2Foam" developed by Jacobsen et al. (2012), is utilized to generate/absorb waves and simulate the interactions between waves and structures. The so-called "relaxation zone" technique is adopted in the waves2Foam toolbox to generate and absorb waves.

The two-phase flow solver, "interFoam", solves the incompressible Navier−Stokes equations to describe the motion of the fluid continuum. To track the interface between the water and the air, the volume of fluid (VOF) method has been employed. The motion of the floating body is solved based on the Newton's second law. The mesh motion of the computational domain is calculated by solving the cell-center Laplace smoothing equation (Jasak and Tuković, 2006). More detailed descriptions on the governing equations and solution methods for the "interFoam" solver, the VOF method, and the motions of both the floating body and the computational mesh can be found in Gao et al.

(2021).

2.2 Generation principles of incident focused wave groups

The incident focused wave groups consist of numerous cosine wave components with varying frequencies that focus at a specific spatial location and moment in time. The free surface elevation of a focused wave group at any spatial position and moment can be expressed as (Chen et al., 2014; Liang et al., 2020):

$$\eta(x,\ t)=\sum_{n=1}^{N}a_n\cos\varphi_n, \tag{1}$$

where

$$a_n=A_{\mathrm{f}}\frac{S(\omega_n)\cdot\Delta\omega}{\sum_{n=1}^{N}S(\omega_n)\cdot\Delta\omega}, \tag{2}$$

$$\varphi_n=k_n(x-x_{\mathrm{f}})-\omega_n(t-t_{\mathrm{f}}). \tag{3}$$

N=100 denotes the total number of the cosine wave components. A_{f} denotes the focused wave amplitude appearing at x=x_{f} and t=t_{f}, and its magnitude would be artificially prescribed based on the research requirements. a_n, ω_n, and k_n denote the wave amplitude, circular frequency, and wavenumber of the n-th cosine wave component, respectively. $\Delta\omega$ denotes the frequency difference between neighboring components. x_{f} and t_{f} denote the desired focusing position and moment, respectively.

The JONSWAP wave energy spectrum is utilized:

$$S(\omega_n)=\alpha g^2\frac{1}{\omega_n^5}\exp\left[-\frac{5}{4}\left(\frac{\omega_{\mathrm{p}}}{\omega_n}\right)^4\right]\gamma^{\beta}, \tag{4}$$

where α=0.0081 and

$$\beta=\exp\left[-\left(\omega_n-\omega_{\mathrm{p}}\right)^2\Big/\left(2\sigma^2\omega_{\mathrm{p}}^2\right)\right]. \tag{5}$$

ω_{p}=2π/T_{p} is the spectral peak circular frequency, and T_{p} is the spectral peak period. σ=0.07 when $\omega_n\leqslant\omega_{\mathrm{p}}$ and otherwise σ=0.09. γ is the peak enhancement factor and is set to 3.3 in this article.

It should be noted that the iterative technique developed by Fernández et al. (2014), which corrects both wave amplitude and phase, has also been adopted, which ensures that the generated focused wave group achieves the desired focused amplitude at the desired position with high precision. For brevity, the detailed principle of this technique is not described here. Interested readers can refer to Fernández et al. (2014) and Gao et al. (2020c) for more information.

3 Numerical wave tank

3.1 Boundary conditions

In this study, the weather-side floater (i.e., Box A) remains fixed, while the lee-side floater (i.e., Box B) is allowed to heave freely under wave actions (see Fig. 1). This layout will be referred to as "heave-box system" for short hereafter. For comparison purposes, the two-box system with both floaters fixed (referred to as "fixed-box system" for short) is also considered, and its interaction with incident focused waves is simulated as control groups.

The wave inlet boundary sets the pressure gradient to zero and prescribes both the water surface elevation and the water particle velocities according to desired wave theories. The outlet boundary set the water particle velocity to zero. For all the solid-wall-type boundaries (including all edges of Box A and the bottom of the numerical wave tank), their velocity boundary condition is set to "no-slip". For the fixed-box system, the velocity boundary condition of Box B is still defined as "no-slip"; while for the heave box system, it is defined as "movingWallVelocity". To absorb the energy of both the reflected and the transmitted waves, two relaxation zones are arranged around the inlet/outlet boundaries. The upper boundary of the numerical wave tank adopts the "atmosphere" boundary condition. For both the front and the back boundaries, the "empty" boundary condition is prescribed to create a 2D numerical wave tank. As in Yin et al. (2022), the largest Courant number is set to 0.25 in all cases to ensure the stability of the simulations and the accuracy of the results.

3.2 Geometric layouts and incident wave parameters

As shown in Fig. 1, a Cartesian coordinate system is defined in the numerical wave tank. The length and the height of the numerical wave tank are 18.5 m and 0.9 m, respectively. Only one cell with the width of W=0.02 m is arranged along the y axis (which is perpendicular to the x-z plane but not shown in the figure). Two identical boxes are deployed in the middle of the wave tank. As stated above,

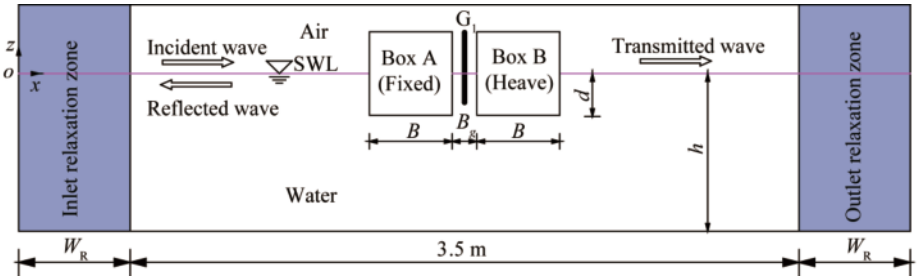

Fig. 1. Sketch of the numerical wave tank used for the heave-box system.

two types of structure layouts (i.e., the heave-box system and the fixed-box system) are considered in the present study. For the heave-box system, the density of Box B is set to 500 kg/m^3. The height H, the breadth B, and the draft d of both boxes are 0.50 m, 0.50 m, and 0.25 m, respectively. The gap width is B_g=0.05 m. The still water depth is h= 0.50 m.

Two built-in mesh-making utilities, "blockMesh" and "snappyHexMesh" are adopted to generate meshes. Typical mesh configurations around the central region for the two numerical wave tanks without and with the two-box system are illustrated in Fig. 2. Along the z-axial direction, to simulate the incident wave groups accurately, the mesh resolution becomes higher and higher from the bottom/atmosphere boundaries to the still water level (SWL). Along the x-axial direction, finer meshes are deployed near the two-box system, especially inside the gap. For the two numerical wave tanks, all mesh configurations are the same except that the meshes within boxes are further removed by using "snappyHexMesh" for the heave-box system.

The geometric configurations for both the still water depth and the two-box system shown in Fig. 1 are identical to the corresponding ones in Saitoh et al. (2006) where the gap resonance of the fixed-box system excited by regular waves was experimentally investigated. Based on Saitoh et al. (2006), the resonant period of the fluid inside the narrow gap for the fixed-box system is T_m = 1.189 s. For the heave-box system considered, the resonant period of the fluid inside the narrow gap is still unknown. To reveal the resonant period of the fluid within the gap for the heave-box system, the spectral peak period of the incident wave trains, T_p, changes from $0.8T_m$ to $1.9T_m$. Five focused wave amplitudes (i.e., A_f/h=0.01, 0.02, 0.03, 0.04 and 0.05) are considered for both types of structural systems. One wave gauge (i.e., G_1) is deployed in the middle of the narrow gap to measure the wave elevation therein. The desired focusing time, t_f, is set to 10.0 s, and the desired focusing position, x_f, is assigned at gauge G_1 (i.e., x_f =9.25 m). The length of each relaxation zone is W_R=7.5 m.

3.3 Validation of mesh convergence

To check the mesh convergence, three meshes with various resolutions (i.e. Meshes 1, 2 and 3) are adopted. The numbers of the cells in Meshes 1−3 are 3.87×10^5, 5.38×10^5 and 8.87×10^5, respectively. Fig. 3 compares the time histories of the wave elevations at gauge G_1 under the three meshes for the two numerical wave tanks without the two-box system and with the heave-box system. The incident focused wave group considered in this figure has A_f/h=0.05 and T_p/T_m=1.3. For Meshes 1 and 2, slight differences appear in the wave elevations at the focusing crest and the adjacent troughs. As the mesh resolution becomes higher, the wave elevations for

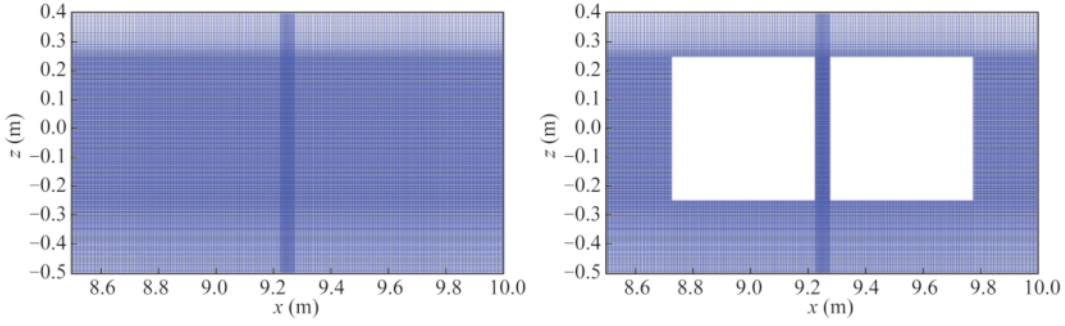

Fig. 2. Typical mesh configurations around the central region for the two numerical wave tanks without and with the two-box system.

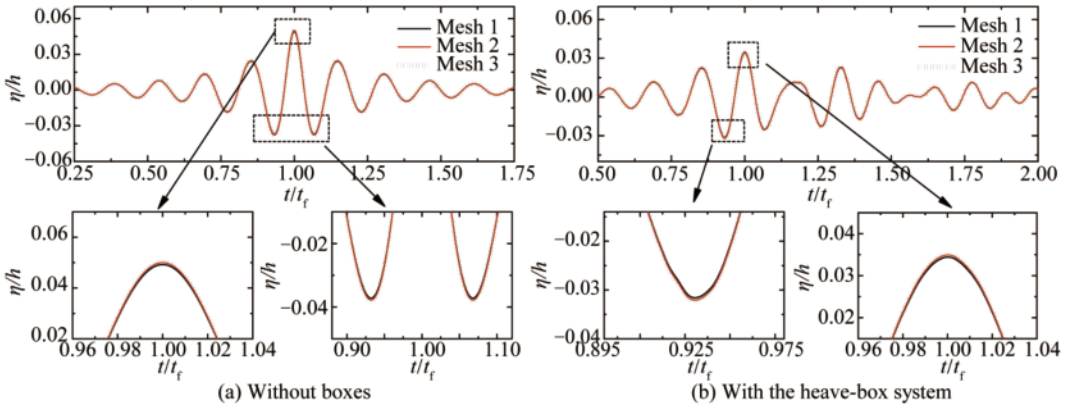

Fig. 3. Comparison of the wave elevations at gauge G_1 under Meshes 1−3 subjected to the incident focused wave group with A_f/h=0.05 and T_p/T_m=1.3 for the numerical wave tanks.

Meshes 2 and 3 become almost overlapped with each other. It shows that the wave elevation has obtained the convergent result for Mesh 2.

Fig. 4 further presents the variations of both the maximum wave elevation inside the gap and the maximum horizontal and vertical wave forces acting on both boxes with respect to the number of the mesh cells for the case shown in Fig. 3b. In this figure, $\zeta_{\mathrm{m}}^{\mathrm{H}}$ denotes the maximum wave elevation within the gap during the entire simulation for the heave-box system. $(F_x^{\mathrm{A}})_{\mathrm{m}}$ and $(F_x^{\mathrm{B}})_{\mathrm{m}}$ denote the maximum horizontal wave forces during the entire simulation acting on Boxes A and B, respectively; $(F_z^{\mathrm{A}})_{\mathrm{m}}$ and $(F_z^{\mathrm{B}})_{\mathrm{m}}$ denote the maximum vertical wave forces on the corresponding boxes. Their specific definitions will be elaborated in Subsections 4.1, 4.3 and 4.4. It is also found that the magnitudes of all the five physical quantities reach convergence for Mesh 2. Hence, Mesh 2 is chosen for all simulations.

It is worth noting that previous studies have extensively validated the capabilities of the numerical model in accurately simulating incident focused wave groups, gap resonance, wave forces, and heave motion of floaters (e.g., Ding and Zang, 2022; Feng et al., 2017; Gao et al., 2019b, 2021, 2022; Wang et al., 2023). Hence, no additional verification is conducted in this study.

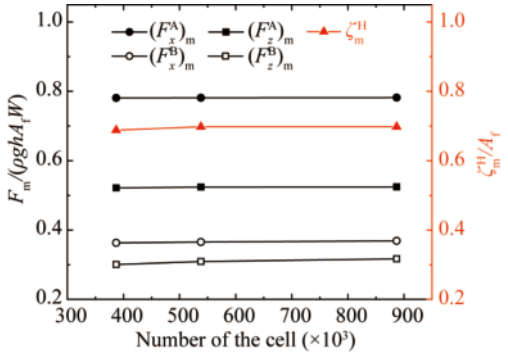

Fig. 4. Variations of both the maximum wave amplification and horizontal/vertical wave forces acting on both boxes with respect to the number of the mesh cells for the case in Fig. 3b.

4 Results and discussion

4.1 Wave amplification in the gap

To compare the fluid resonance characteristics between the heave- and the fixed-box systems, Fig. 5 presents the time histories of wave elevations at gauge G_1 for both structural systems, and the corresponding amplification factors of the wave elevation in the gap are also shown in the figure. Two distinct differences can be observed from the results. Firstly, the amplification factor of the wave elevation for the heave-box system (i.e., $\zeta_{\mathrm{m}}^{\mathrm{H}}/A_{\mathrm{f}}$) is always notably lower than the corresponding one for the fixed-box system (i.e., $\zeta_{\mathrm{m}}^{\mathrm{F}}/A_{\mathrm{f}}$). This can be qualitatively attributed to the fact that part of the incident wave energy is converted into the mechanical energy for the floater motion in the heave-box system. Secondly, there exists significant difference for the fluid resonant period between the two types of structural systems. For the fixed-box system, the maximum amplification factor of the wave elevation always appears at $T_{\mathrm{p}}/T_{\mathrm{m}}$=1.0, no matter whether A_{f} is large or small; while for the heave-box system, it always appears at $T_{\mathrm{p}}/T_{\mathrm{m}}$=1.7. It indicates that the fluid res-

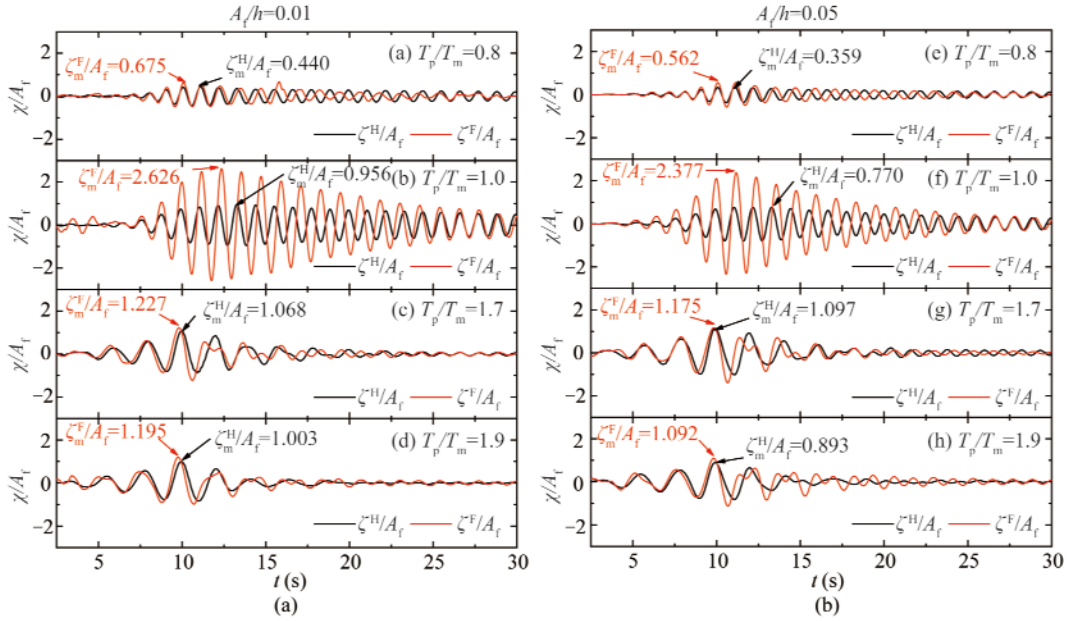

Fig. 5. Time histories of the wave elevations at G_1 for both the heave- and the fixed-box systems suffering from the incident wave groups with various A_{f} and T_{p}. (a–d) and (e–h) correspond to the incident wave groups with A_{f}/h=0.01 and 0.05, respectively. ζ^{H} and ζ^{F} denote the wave elevations for the heave- and the fixed-box systems, respectively. The subscript "m" represents their respective maximums during the entire simulation. The symbol "χ" represents ζ^{H} or ζ^{F}.

onant period of the heave-box system becomes notably larger than that of the fixed-box system. In fact, the remarkable decline of the wave amplification factor and the obvious change of the fluid resonant period due to the floater motion have also been observed in the steady-state gap resonance investigations (e.g., Fredriksen et al. (2015); He et al. (2022)).

Fig. 6 presents the changing trends of the amplification factor of the wave elevation with T_p for both the heave- and the fixed-box systems under all the five focused wave amplitudes. Four phenomena are clearly seen. Firstly, the release of the heave DoF of Box B indeed causes quite different features for the transient gap resonance. For the fixed-box system, the maximum amplification factor appears at T_p=T_m. While for the heave-box system, the fluid resonant period that corresponds to the maximum amplification factor shifts upwards to T_p=1.7T_m, regardless of the incident focused wave amplitude. Secondly, for the heave-box system, although its fluid resonant period becomes remarkably larger than that of the fixed-box system, there still exists a local peak point of the amplification factor at T_p≈0.95T_m whose value is only slightly lower than the corresponding maximum value at T_p=1.7T_m (more intuitive comparison between them will be presented in Fig. 7). It implies that the fluid resonant period of the fixed-box system still has a significant influence on the transient resonance characteristics of the heave-box system.

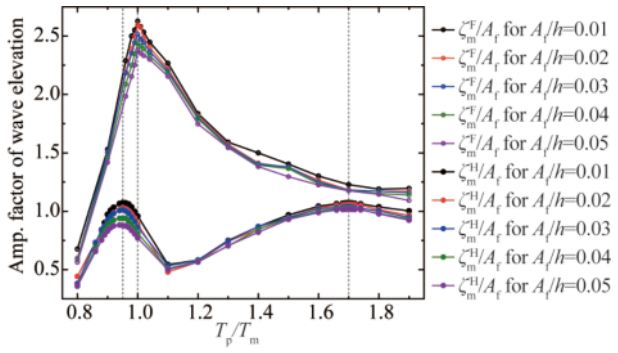

Fig. 6. Changing trends of the amplification factor of wave elevation within the gap with respect to the spectral peak period for both the heave- and the fixed-box systems.

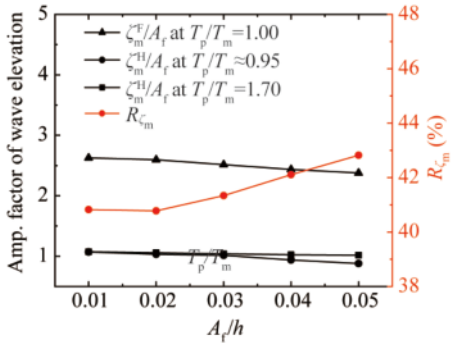

Fig. 7. Comparisons of the maximum (and the local peak) amplification factors of wave elevations between the heave- and the fixed-box systems, where $R_{\zeta m}$ denotes the ratio of ζ_m^H at T_p/T_m=1.70 to ζ_m^F at T_p/T_m=1.00.

Thirdly, for both structural systems, their maximum amplification factors of wave elevations at the fluid resonant periods and the local peak amplification factors at T_p≈0.95T_m (for the heave-box system only) are shown to monotonously decrease with the rise of A_f (also see Fig. 7). Fourthly, the maximum amplification factor of wave elevation for the heave-box system (i.e., ζ_m^H/A_f at T_p=1.70T_m) is remarkably smaller than the corresponding one for the fixed-box system (i.e., ζ_m^F/A_f at T_p=T_m). As mentioned above, this is because a portion of the incident wave energy is converted into the mechanical energy for the floater motion in the heave-box system. The ratio between them, $R_{\zeta m}$, is also calculated and shown in Fig. 7. It is observed that $R_{\zeta m}$ gradually increases with A_f overall. The maximum $R_{\zeta m}$ is only 42.8%, appearing at A_f/h=0.05.

4.2 Heave motion of the lee-side box

To present the heave motion characteristics of the lee-side box in the heave-box system, the time histories of the heave displacement of Box B, Γ, subjected to the incident focused wave groups with various spectral peak periods and with A_f/h=0.01 and 0.05 are shown in Fig. 8. It is seen that for both A_f/h=0.01 and 0.05, the heave motion of Box B becomes more and more significant as the spectral peak period, T_p, increases from 0.8T_m to 1.6T_m, and then the former decreases slightly when T_p further rises to 1.9T_m. Among the four spectral peak periods, the maximum Γ_m appears at T_p =1.6T_m for both A_f/h=0.01 and 0.05 (see Figs. 8c and 8g).

To reveal the influence of the spectral peak period on the heave motion of the lee-side box more comprehensively, Fig. 9 further presents the changing trends of the maximum heave displacement of Box B during the entire simulation (i.e., Γ_m) with respect to T_p. It is seen that Γ_m monotonically increases first and then monotonically decreases with T_p, and the maximum value of Γ_m/A_f always occurs at T_p/T_m = 1.6, regardless of the incident focused wave amplitude. In addition, the normalized Γ_m (i.e., Γ_m/A_f) is shown to decrease gradually with the increase of the incident focused wave amplitude, regardless of the spectral peak period.

A possible reason for both phenomena can be explained as follows. Aiming at the heave-box system, Gao et al. (2021) has implemented a free decay test and found that the resonant period of the heave motion is T_h=1.667 s (i.e., T_p/T_m =1.40). Based on the results shown in Subsection 4.1, the fluid resonance inside the gap always appears at T_p/T_m= 1.70. Compared with the resonant period of the heave motion, the fluid resonant period inside the gap is closer to T_p/T_m =1.60 where the maximum heave motion occurs. Furthermore, the phenomenon that Γ_m/A_f decreases monotonically with A_f is well consistent with the corresponding phenomenon that ζ_m^H/A_f at T_p/T_m=1.70 decreases gradually with

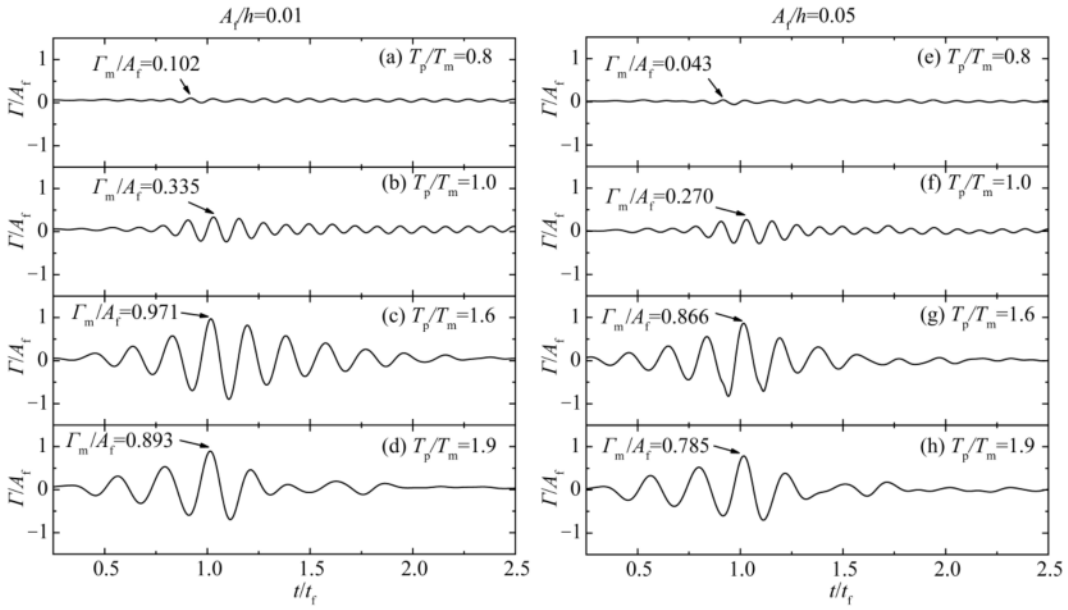

Fig. 8. Time histories of the heave displacement of Box B, Γ, in the heave-box system subjected to the incident focused wave groups with various A_f and T_p. (a−d) and (e−h) correspond to the incident wave groups with A_f/h=0.01 and 0.05, respectively. Γ_m denotes the maximum heave displacement during the entire simulation.

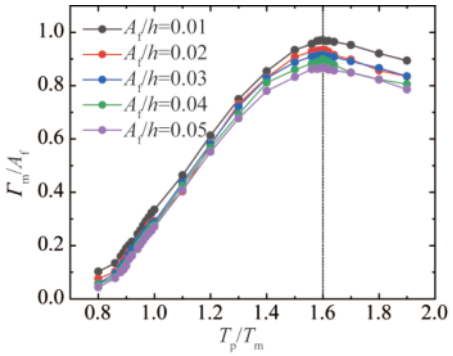

Fig. 9. Tendencies of the normalized maximum heave displacement of Box B (i.e., Γ_m/A_f) with respect to T_p for the heave-box system

A_f shown in Fig. 7. Based on the two aspects mentioned above, it can be inferred that the heave motion characteristics of Box B primarily rely on the fluid resonance characteristics within the gap and that the resonant heave motion is a relatively insignificant factor.

4.3 Horizontal wave forces

Fig. 10 depicts the comparisons of the time histories of horizontal wave forces acting on both boxes in the heave-box system subjected to the incident focused waves with A_f/h=0.01 and 0.05, where the wave forces are normalized by $\rho g h A_f W$. For each set of A_f and T_p, the maximum horizontal forces during the entire simulation acting on Boxes A and B are defined as:

$$\left(F_x^{\mathrm{A}}\right)_{\mathrm{m}} = \max\left(\left(F_{+x}^{\mathrm{A}}\right)_{\mathrm{m}}, \left|\left(F_{-x}^{\mathrm{A}}\right)_{\mathrm{m}}\right|\right), \tag{6}$$

and

$$\left(F_x^{\mathrm{B}}\right)_{\mathrm{m}} = \max\left(\left(F_{+x}^{\mathrm{B}}\right)_{\mathrm{m}}, \left|\left(F_{-x}^{\mathrm{B}}\right)_{\mathrm{m}}\right|\right), \tag{7}$$

respectively. $\left(F_{+x}^{\mathrm{A}}\right)_{\mathrm{m}}$ and $\left(F_{+x}^{\mathrm{B}}\right)_{\mathrm{m}}$ respectively denote the maximum horizontal forces acting on Boxes A and B in the +x-axial direction during the entire simulation, and $\left(F_{-x}^{\mathrm{A}}\right)_{\mathrm{m}}$ and $\left(F_{-x}^{\mathrm{B}}\right)_{\mathrm{m}}$ denote the corresponding maximum ones in the –x-axial direction. All the four parameters are directly read from the time histories of horizontal wave forces, and their specific values are also marked out in this figure. It is seen from this figure that for the heave-box system, the maximum horizontal wave force on Box A is shown to first increase and then decrease with the rise of the spectral peak period, regardless of the incident focused wave amplitude. Nevertheless, the maximum horizontal wave force on Box B seems to gradually increase with the spectral peak period.

The tendencies of the maximum horizontal wave forces with respect to T_p for both the heave- and the fixed-box systems with A_f/h=0.01, 0.03 and 0.05 are illustrated in Fig. 11 more comprehensively. As stated above, for the heave-box system, the maximum horizontal force on Box A first increases and then decreases with T_p overall, and its maximum value within the whole range of T_p [denoted by $(E_x^{\mathrm{A}})_{\mathrm{m}}$] always appears at T_p=1.3T_m. The maximum horizontal force on Box B presents a gradual increasing trend with T_p, and its maximum value within the whole range of T_p [denoted by $(E_x^{\mathrm{B}})_{\mathrm{m}}$] occurs at T_p=1.8T_m or 1.9T_m. In addition, like the local peak of the amplification factor of the wave elevation appearing at T_p≈0.95T_m (see Fig. 6), there also exist local peaks at T_p≈0.9T_m or 0.95T_m for the two curves of the maximum horizontal wave forces acting on both boxes. It also indicates that the fluid resonant period of the fixed-box system

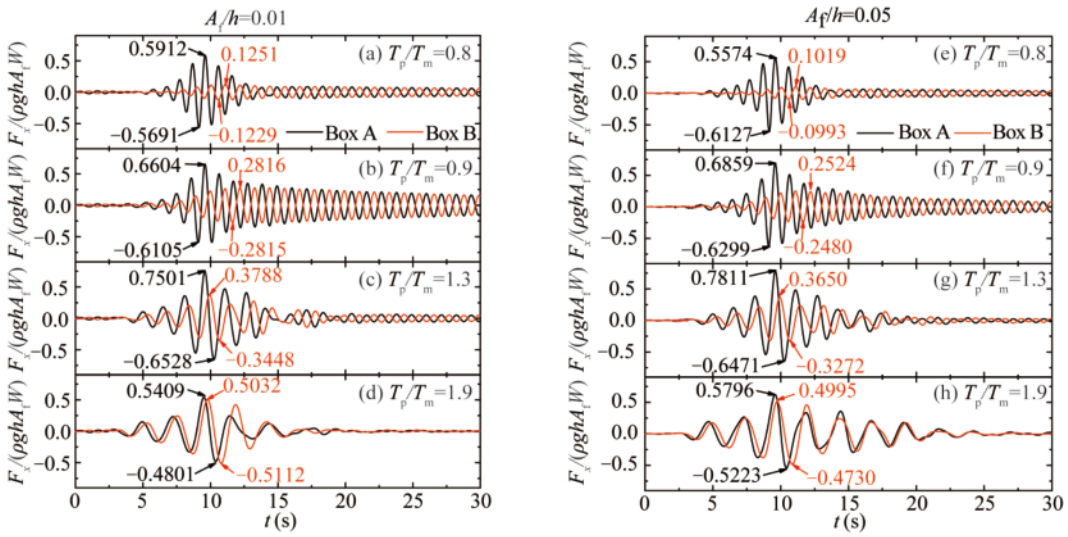

Fig. 10. Comparisons of the time histories of horizontal wave forces acting on both boxes in the heave-box system subjected to the focused waves with various sets of A_f and T_p. (a–d) and (e–h) correspond to the cases with A_f/h=0.01 and 0.05, respectively. The magnitudes marked out in each sub-figure denote the respective maximums in the $+x$- or $-x$-axial directions.

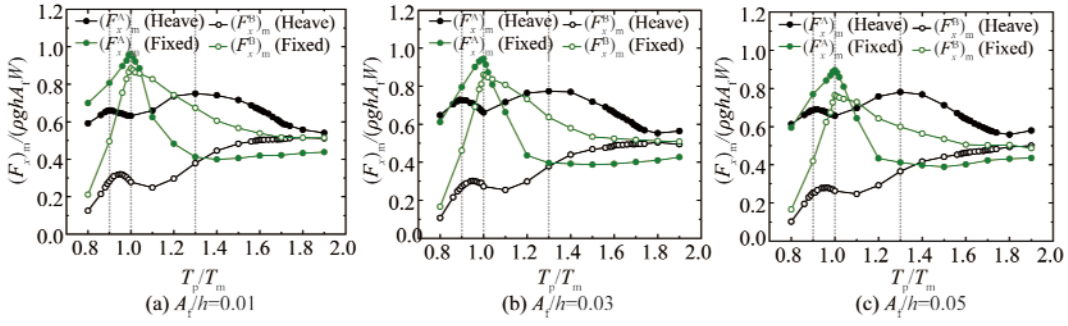

Fig. 11. Tendencies of the maximum horizontal wave forces acting on Boxes A and B with respect to T_p for both structural systems under the conditions of (a) A_f/h=0.01, (b) A_f/h=0.03 and (c) A_f/h=0.05. The symbol "$(F_x)_m$" in the figure represents $(F_x^A)_m$ or $(F_x^B)_m$.

still has a notable influence on the heave-box system. However, the changing trends of the maximum horizontal wave forces with T_p for the fixed-box system are quite different from those for the heave-box system. Specifically speaking, for the fixed-box system, the maximum horizontal force on Box A is shown to first sharply increase, then sharply decrease, and finally increase very gently with the increase of T_p, and the maximum horizontal force on Box B is shown to first sharply ascend and then decline relatively gently. Their maximum values within the whole range of T_p always strictly occur at T_p=T_m.

Besides the phenomena described above, it can also be seen from Fig. 10 that for the heave-box system, when the spectral peak period, T_p, is small (i.e., T_p=0.8T_m in Fig. 10a and e), the maximum horizontal wave forces on Box B are remarkably lower than the corresponding ones on Box A, regardless of the incident focused wave amplitude. It indicates that Box A has significant shielding effect on Box B under this condition. As T_p increases, although the maximum horizontal wave forces on Box B are still smaller than the corresponding ones on Box A, the former is getting closer and closer to the latter. When T_p/T_m increases to 1.9, the normalized maximum horizontal forces on Boxes B and A for the case with A_f/h=0.01 are 0.511 and 0.541, respectively (see Fig. 10d), and the ratio of the former to the latter is 94.51%; the normalized maximum horizontal forces on Boxes B and A for the case with A_f/h=0.05 are 0.500 and 0.580, respectively (see Fig. 10h), and the ratio of the former to the latter is 86.18%.

To better present this phenomenon, the ratios of the maximum horizontal wave forces on Box B to the corresponding ones on Box A for the heave-box system are systematically shown in Fig. 12. For comparison, the ratios for the fixed-box system are also illustrated in the figure. It is easily found that for the heave-box system, the ratio of the maximum horizontal force gradually increases from around 20% to around 90% with T_p/T_m increasing from 0.8 to 1.9. Nevertheless, the ratio for the fixed-box system is entirely different from that for the heave-box system. The ratio for the fixed-box system first monotonically increases and then

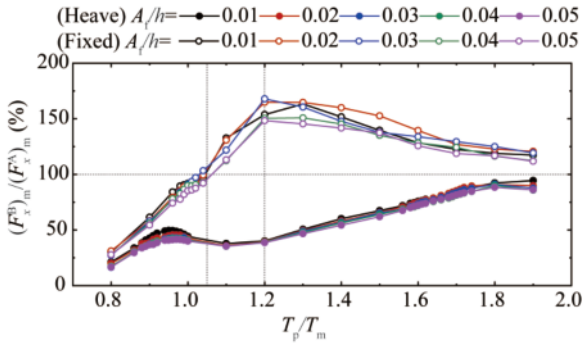

Fig. 12. Ratios of the maximum horizontal forces acting on Box B to the corresponding ones acting on Box A for all cases of both the heave- and the fixed-box systems.

gradually decreases with T_p. When T_p/T_m exceeds about 1.05, the ratio becomes larger than 100%, which means that the weather-side box can no longer provide shielding effect on the lee-side box. The maximum ratios for the fixed-box system always appear at T_p/T_m≈1.20, and their magnitudes vary from 148.4% to 167.9%, depending on the incident focused wave amplitude. For both structural systems, the minimum ratios that represent the best shielding effect of the weather-side fixed box on the lee-side box always appears at the lowest incident wave period (i.e., T_p/T_m=0.8).

To understand how the incident focused wave amplitude, A_f, affects the maximum horizontal wave forces within the whole range of T_p [i.e., $(E_x^A)_m$ and $(E_x^B)_m$] in both the heave- and the fixed-box systems, Fig. 13 shows the changing trends of the normalized $(E_x^A)_m$ and $(E_x^B)_m$ [i.e., $(E_x^A)_m/(\rho g h A_f W)$ and $(E_x^B)_m/(\rho g h A_f W)$] with respect to A_f. Two phenomena are easily observed. Firstly, except $(E_x^A)_m$ in the heave-box system, all the other three variables, including the normalized $(E_x^B)_m$ in the heave-box system and both the normalized $(E_x^A)_m$ and $(E_x^B)_m$ in the fixed-box system, are shown to gradually decrease with A_f. Contrarily, for the normalized $(E_x^A)_m$ in the heave-box system, it shows a gradual upward trend with A_f.

Secondly, for both boxes, the maximum horizontal wave forces within the whole range of T_p in the heave-box system

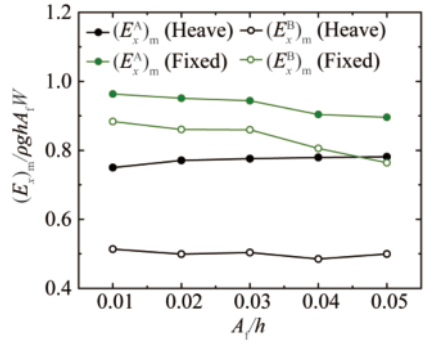

Fig. 13. Tendencies of the normalized maximum horizontal wave forces within the whole range of T_p with respect to A_f for both the heave- and the fixed-box systems. $(E_x)_m$ represents $(E_x^A)_m$ or $(E_x^B)_m$.

are always notably lower than the corresponding ones in the fixed-box system. To quantitatively describe the phenomenon, both the ratio of $(E_x^A)_m$ in the heave-box system to the corresponding one in the fixed-box system (denoted by R_{Fx}^A) and the ratio of the $(E_x^B)_m$ in the heave-box system to the corresponding one in the fixed-box system (denoted by R_{Fx}^B) are further calculated and presented in Fig. 14 for all the five incident focused wave amplitudes considered. It shows that both R_{Fx}^A and R_{Fx}^B increases monotonously as A_f increases, and their maximum values are respectively 87.2% and 65.4%, appearing at A_f/h=0.05.

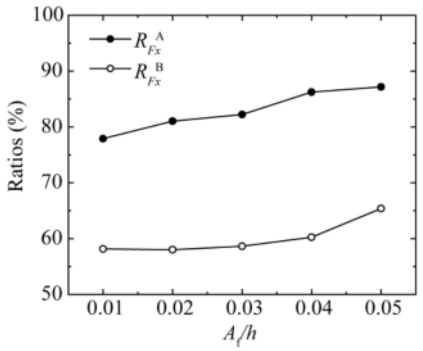

Fig. 14. Variations of R_{Fx}^A and R_{Fx}^B with respect to A_f.

4.4 Vertical wave forces

For each set of T_p and A_f, the maximum vertical wave forces during the entire simulation on the weather- and the lee-side boxes are defined as:

$$\left(F_z^A\right)_m = \max\left(\left(F_{+z}^A\right)_m, \left|\left(F_{-z}^A\right)_m\right|\right) \tag{8}$$

and

$$\left(F_z^B\right)_m = \max\left(\left(F_{+z}^B\right)_m, \left|\left(F_{-z}^B\right)_m\right|\right), \tag{9}$$

respectively. $\left(F_{+z}^A\right)_m$ and $\left(F_{+z}^B\right)_m$ denote the maximum vertical forces on Boxes A and B in $+z$-axial directions during the entire simulation, respectively; $\left(F_{-z}^A\right)_m$ and $\left(F_{-z}^B\right)_m$ denote the corresponding maximums in $-z$-axial directions. Their specific magnitudes can be directly gained from the time histories of the vertical wave forces.

The tendencies of the maximum vertical forces during the entire simulation with respect to T_p for both structural systems are shown in Fig. 15. It is observed that not only $(F_z^A)_m$ in the heave-box system but also both $(F_z^A)_m$ and $(F_z^B)_m$ in the fixed-box system present a gradual increasing tendency with the rise of T_p. However, for $(F_z^B)_m$ in the heave-box system, it first monotonously increases and then monotonously decreases with T_p, and its maximum value within the whole range of T_p [denoted by $(E_z^B)_m$] always occurs at T_p/T_m=1.4. Furthermore, the magnitude of $(F_z^B)_m$ is always notably lower than that of the corresponding $(F_z^A)_m$, regardless of the incident wave amplitude and the type of

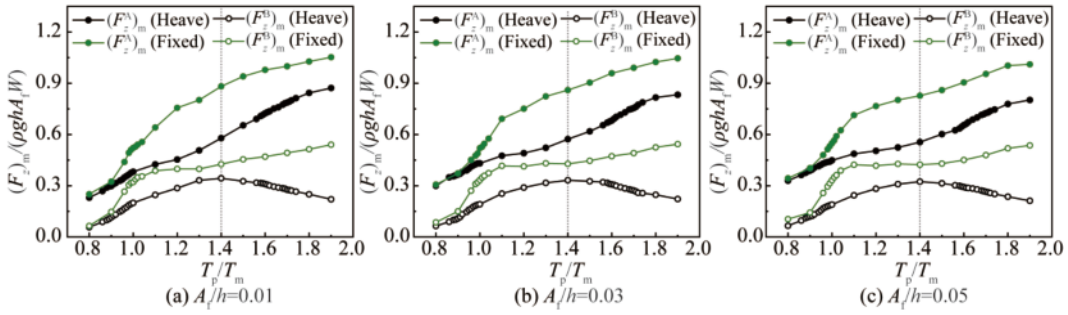

Fig. 15. Variations of the maximum vertical wave forces with T_p for both structural systems under (a) A_f/h=0.01, (b) A_f/h=0.03 and (c) A_f/h=0.05. $(F_z)_m$ in the figure represents $(F_z^A)_m$ or $(F_z^B)_m$.

structural system. It indicates that in terms of the vertical wave force, the weather-side fixed box (i.e., Box A) always plays a pretty good shielding role on the lee-side box (i.e., Box B).

To quantitatively investigate the shielding effect of the weather-side fixed box on the lee-side box, the ratios of $(F_z^B)_m$ to the corresponding $(F_z^A)_m$ for all cases are shown in Fig. 16. It is seen that for both structural systems, the maximum ratios that mean the weakest shielding effect are similar to each other, both around 60%. However, the spectral peak period at which the maximum ratio appears is different for the two structural systems. For the fixed-box system, the maximum ratio always occurs at $T_p/T_m \approx 1.0$; while for the heave-box system, the normalized spectral peak period where the maximum ratio appears shifts upward to 1.3 for all the incident focused wave amplitudes. Identical to the related phenomenon shown in Fig. 12, for the vertical wave forces, the best shielding effect of the weather-side fixed box on the lee-side box also always occurs at the lowest incident wave period (i.e., T_p/T_m=0.8).

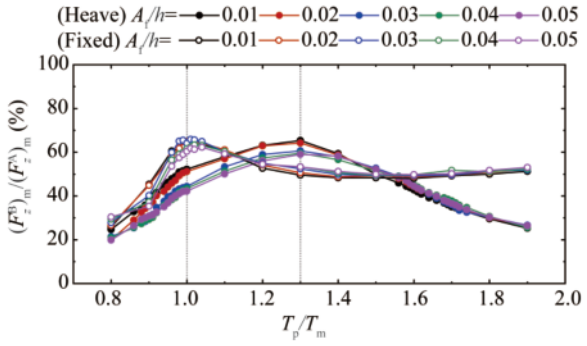

Fig. 16. Ratios of the maximum vertical wave forces on Box B to the corresponding ones on Box A for all cases of both the heave- and the fixed-structural systems.

To reveal how the incident focused wave amplitude influences the maximum vertical wave forces within the whole range of T_p [denoted by $(E_z^A)_m$ and $(E_z^B)_m$] in both structural systems, their variations with A_f are presented in Fig. 17, where both $(E_z^A)_m$ and $(E_z^B)_m$ are normalized by $\rho g h A_f W$. It is seen that all the four normalized variables

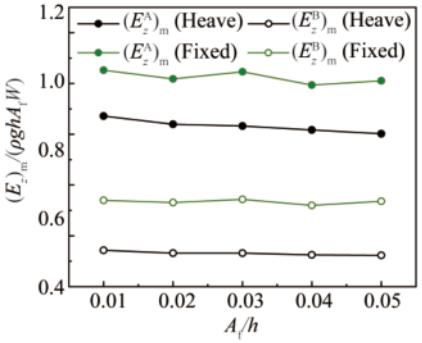

Fig. 17. Variations of the normalized $(E_z^A)_m$ and $(E_z^B)_m$ with A_f in both structural systems. $(E_z^A)_m$ and $(E_z^B)_m$ respectively denote the maximum values of $(F_z^A)_m$ and $(F_z^B)_m$ within the whole range of T_p. $(E_z)_m$ represents $(E_z^A)_m$ or $(E_z^B)_m$.

present a downward trend with the rise of A_f. Furthermore, just like $(E_x^A)_m$ and $(E_x^B)_m$ shown in Fig. 13, both $(E_z^A)_m$ and $(E_z^B)_m$ in the heave-box system are also remarkably lower than the corresponding ones in the fixed-box system. To quantify their differences, the ratio of $(E_z^A)_m$ in the heave-box system to the corresponding one in the fixed-box system (denoted by R_{Fz}^A) and the ratio of $(E_z^B)_m$ in the heave-box system to the corresponding one in the fixed-box system (denoted by R_{Fz}^B) are further calculated and illustrated in Fig. 18. Both R_{Fz}^A and R_{Fz}^B show a slight downward trend with the rise of A_f, and their maximum values are respectively 82.9% and 63.6%, appearing at A_f/h=0.01.

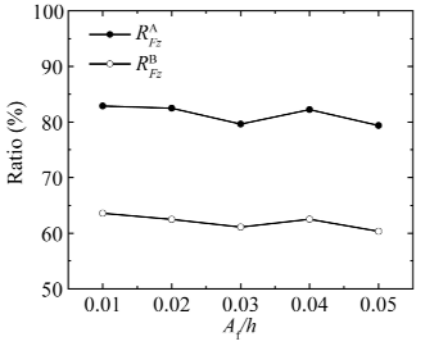

Fig. 18. Variations of R_{Fz}^A and R_{Fz}^B with respect to A_f.

5 Conclusions

In this article, the OpenFOAM model has been used to study the transient gap resonance formed between two boxes triggered by the focused wave groups with various focused wave amplitudes and spectral peak periods. The weather-side box (i.e. Box A) remains stationary. The lee-side box (i.e. Box B) has two different conditions. In the heave-box system, Box B is allowed to heave freely under wave actions; in the fixed-box system, it still remains fixed, just like Box A. How the release of the heave DoF of Box B affects the gap resonance characteristics is revealed. The effects of both the focused wave amplitude and the spectral peak period on the wave amplification inside the gap, the heave displacement of Box B, and the wave forces on both boxes are studied as well. Based on the research results, the following conclusions can be drawn:

(1) The release of the heave DoF of Box B brings about remarkably different features for the wave amplification. The fluid resonant period of the heave-box system becomes 1.7 times that of the fixed-box system. However, the wave amplification factor inside the gap in the heave-box system becomes significantly lower than that in the fixed-box one. The maximum heave displacement of Box B always appears at T_p/T_m=1.6, regardless of the incident focused wave amplitude.

(2) The heave motion of Box B causes different characteristics for both the horizontal and the vertical wave forces as well. In the heave-box system, the maximum horizontal force on Box A within the whole range of T_p [i.e., $(E_x^A)_m$] and that on Box B [i.e., $(E_x^B)_m$] always appear at T_p/T_m= 1.3 and 1.9, respectively, while in the fixed-box system, both always occur at T_p/T_m =1.0. For the vertical wave forces, the maxima acting on both boxes in the fixed-box system [i.e., $(E_z^A)_m$ and $(E_z^B)_m$] occurs at T_p/T_m=1.9. However, $(E_z^B)_m$ in the heave-box system appears at T_p/T_m=1.4, although $(E_z^A)_m$ still appears at T_p/T_m=1.9.

(3) In terms of the horizontal force, Box A can provide shielding effect on Box B within the whole range of T_p in the heave-box system, and the shielding effect becomes weaker and weaker as T_p rises. However, in the fixed-box system, Box A can provide shielding effect on Box B only when T_p/T_m<1.05. In terms of the vertical wave force, Box A plays a pretty good shielding role on Box B within the whole range of T_p in both structural systems.

(4) Except the normalized maximum horizontal wave forces within the whole range of T_p acting on Box A [i.e., $(E_x^A)_m/(\rho g h A_f W)$] in the heave-box system, all the other nine normalized physical quantities concerned [i.e., the maximum wave amplification factor, $(E_x^B)_m/(\rho g h A_f W)$, $(E_z^A)_m/(\rho g h A_f W)$ and $(E_z^B)_m/(\rho g h A_f W)$ in both structural systems, and $(E_x^A)_m/(\rho g h A_f W)$ in the fixed-box system] show a downward trend with the incident focused wave amplitude. On the contrary, $(E_x^A)_m/(\rho g h A_f W)$ in the heave-box system shows an upward trend with the latter.

Finally, it is reaffirmed here that all the results and conclusions obtained in the present study are only applicable to the given geometric layout and the given incident focused wave groups considered in this paper.

Competing interests

The authors declare no competing interests.

References

Chen, L.F., Zang, J., Hillis, A.J., Morgan, G.C.J. and Plummer, A.R., 2014. Numerical investigation of wave-structure interaction using OpenFOAM, *Ocean Engineering*, 88, 91–109.

Cong, P.W., Teng, B., Gou, Y., Tan, L. and Liu, Y.Y., 2022. Hydrodynamic analysis of resonant waves within the gap between a vessel and a vertical quay wall, *Ocean Engineering*, 260, 112192.

Ding, Y.F., Walther, J.H. and Shao, Y.L., 2022a. Higher-order gap resonance and heave response of two side-by-side barges under Stokes and cnoidal waves, *Ocean Engineering*, 266, 112835.

Ding, Y.F., Walther, J.H. and Shao, Y.L., 2022b. Higher-order gap resonance between two identical fixed barges: A study on the effect of water depth, *Physics of Fluids*, 34(5), 052113.

Ding, H.Y. and Zang, J., 2022. Numerical investigation of the survivability of a wave energy converter, *Proceedings of the 37th International Workshop on Water Waves and Floating Bodies*, Giardini Naxos, Italy.

Eatock Taylor, R., Sun, L. and Taylor, P.H., 2008. Gap resonances in focused wave groups, *Proceedings of the 23rd International Workshop on Water Waves and Floating Bodies*, Jeju, Korea.

Fan, J., Tao, A.F., Xie, S.Y., Wu, D. and Wang, G., 2023. Numerical investigation on nonlinear evolution behavior and water particle velocity of wave crests for narrow-band wave field with Gaussian spectrum, *Ocean Engineering*, 268, 113518.

Feng, A.C., Magee, A. and Price, W.G., 2020. Experimental and numerical study for drillship moonpool gap resonances in stationary and transit conditions in wave flume, *Journal of Offshore Mechanics and Arctic Engineering*, 142(2), 021205.

Feng, X., Bai, W., Chen, X.B., Qian, L. and Ma, Z.H., 2017. Numerical investigation of viscous effects on the gap resonance between side-by-side barges, *Ocean Engineering*, 145, 44–58.

Fernández, H., Sriram, V., Schimmels, S. and Oumeraci, H., 2014. Extreme wave generation using self correcting method-Revisited, *Coastal Engineering*, 93, 15–31.

Fredriksen, A.G., Kristiansen, T. and Faltinsen, O.M., 2015. Wave-induced response of a floating two-dimensional body with a moonpool, *Philosophical Transactions of the Royal Society A Mathematical, Physical and Engineering Sciences*, 373(2033), 20140109.

Fu, R.L., Ma, Y.X., Dong, G.H. and Perlin, M., 2021. A wavelet-based wave group detector and predictor of extreme events over unidirectional sloping bathymetry, *Ocean Engineering*, 229, 108936.

Gao, J.L., Bi, W.J., Zhang, J. and Zang, J., 2023a. Numerical investigations on harbor oscillations induced by falling objects, *China Ocean Engineering*, 37(3), 458–470.

Gao, J.L., Chen, H.Z., Zang, J., Chen, L.F., Wang, G. and Zhu, Y.Z., 2020a. Numerical investigations of gap resonance excited by focused transient wave groups, *Ocean Engineering*, 212, 107628.

Gao, J.L., Gong, S.K., He, Z.W., Shi, H.B., Zang, J., Zou, T. and Bai, X., 2023b. Study on wave loads during steady-state gap resonance with free heave motion of floating structure, *Journal of Marine Science and Engineering*, 11(2), 448.

Gao, J.L., He, Z.W., Huang, X.H., Liu, Q., Zang, J. and Wang, G.,

2021. Effects of free heave motion on wave resonance inside a narrow gap between two boxes under wave actions, *Ocean Engineering*, 224, 108753.

Gao, J.L., He, Z.W., Zang, J., Chen, Q., Ding, H.Y. and Wang, G., 2019a. Topographic effects on wave resonance in the narrow gap between fixed box and vertical wall, *Ocean Engineering*, 180, 97–107.

Gao, J.L., He, Z.W., Zang, J., Chen, Q., Ding, H.Y. and Wang, G., 2020b. Numerical investigations of wave loads on fixed box in front of vertical wall with a narrow gap under wave actions, *Ocean Engineering*, 206, 107323.

Gao, J.L., Lyu, J., Wang, J.H., Zhang, J., Liu, Q., Zang, J. and Zou, T., 2022. Study on transient gap resonance with consideration of the motion of floating body, *China Ocean Engineering*, 36(6), 994–1006.

Gao, J.L., Ma, X.Z., Zang, J., Dong, G.H., Ma, X.J., Zhu, Y.Z. and Zhou, L., 2020c. Numerical investigation of harbor oscillations induced by focused transient wave groups, *Coastal Engineering*, 158, 103670.

Gao, J.L., Shi, H.B., Zang, J. and Liu, Y.Y., 2023c. Mechanism analysis on the mitigation of harbor resonance by periodic undulating topography, *Ocean Engineering*, 281, 114923.

Gao, J.L., Zang, J., Chen, L.F., Chen, Q., Ding, H.Y. and Liu, Y.Y., 2019b. On hydrodynamic characteristics of gap resonance between two fixed bodies in close proximity, *Ocean Engineering*, 173, 28–44.

He, G.H., Jing, P.L., Jin, R.J., Zhang, W., Zhang, J.W. and Liu, T., 2021a. Two-dimensional numerical study on fluid resonance in the narrow gap between two rigid-connected heave boxes in waves, *Applied Ocean Research*, 110, 102628.

He, Y.L., Wu, G.L., Mao, H.F., Chen, H.Z., Lin, J.B. and Dong, G.H., 2023. An experimental study on nonlinear wave dynamics for freak waves over an uneven bottom, *Frontiers in Marine Science*, 10, 1150896.

He, Z.W., Gao, J.L., Chen, H.Z., Zang, J., Liu, Q. and Wang, G., 2021b. Harmonic analyses of hydrodynamic characteristics for gap resonance between fixed box and vertical wall, *China Ocean Engineering*, 35(5), 712–723.

He, Z.W., Gao, J.L., Shi, H.B., Zang, J., Chen, H.Z. and Liu, Q., 2022. Investigation on effects of vertical degree of freedom on gap resonance between two side-by-side boxes under wave actions, *China Ocean Engineering*, 36(3), 403–412.

He, Z.W., Gao, J.L., Zang, J., Chen, H.Z., Liu, Q. and Wang, G., 2021c. Effects of free heave motion on wave forces on two side-by-side boxes in close proximity under wave actions, *China Ocean Engineering*, 35(4), 490–503.

Jacobsen, N.G., Fuhrman, D.R. and Fredsøe, J., 2012. A wave generation toolbox for the open-source CFD library: OpenFoam®, *International Journal for Numerical Methods in Fluids*, 70(9), 1073–1088.

Jasak, H. and Tuković, Z., 2006. Automatic mesh motion for the unstructured finite volume method, *Transactions of FAMENA*, 30(2), 1–20.

Jiang, S.C., Feng, A.C. and Yan, B., 2022. Numerical simulation for internal baffle effect on suppressing sway-sloshing coupled motion response, *Ocean Engineering*, 250, 110513.

Jiang, S.C., Liu, H., Sun, T.Z. and Gu, Q., 2020. Numerical simulation for hydrodynamic behavior of box-systems with and without narrow gaps, *Ocean Engineering*, 214, 107698.

Jiang, S.C., Sun, Z., Feng, A.C. and Zhang, G.Y., 2019. On hydrodynamic behavior of fluid resonance in moonpool and its suppression by using various convex appendages, *Ocean Engineering*, 192, 106552.

Jing, P.L., He, G.H., Luan, Z.X., Liu, C.G. and Yang, H., 2022. Numerical study of fluid resonance of a two-dimensional heaving-free moonpool in a wide range of incident waves, *Journal of Hydrodynamics*, 34(4), 647–664.

Kristiansen, T. and Faltinsen, O.M., 2010. A two-dimensional numerical and experimental study of resonant coupled ship and piston-mode motion, *Applied Ocean Research*, 32(2), 158–176.

Li, X., Xu, L.Y. and Yang, J.M., 2016. Study of fluid resonance between two side-by-side floating barges, *Journal of Hydrodynamics*, 28(5), 767–777.

Li, Y.J., 2019. Fully nonlinear analysis of second-order gap resonance between two floating barges, *Engineering Analysis with Boundary Elements*, 106, 1–19.

Liang, H., Chua, K.H., Wang, H.C. and Choo, Y.S., 2021. Numerical and experimental investigations into fluid resonance in a gap between two side-by-side vessels, *Applied Ocean Research*, 111, 102581.

Liang, H., Liu, X.B., Chua, K.H., De Mello, P.C. and Choo, Y.S., 2022. Wave actions on side-by-side barges with sloshing effects: fixed-free arrangement, *Flow*, 2, E20.

Liang, H., Santo, H., Shao, Y.L., Law, Y.Z. and Chan, E.S., 2020. Liquid sloshing in an upright circular tank under periodic and transient excitations, *Physical Review Fluids*, 5(8), 084801.

Liu, J.S., Gao, J.L., Shi, H.B., Zang, J. and Liu, Q., 2022. Investigations on the second-order transient gap resonance induced by focused wave groups, *Ocean Engineering*, 263, 112430.

Lu, L., Tan, L., Zhou, Z.B., Zhao, M. and Ikoma, T., 2020. Two-dimensional numerical study of gap resonance coupling with motions of floating body moored close to a bottom-mounted wall, *Physics of Fluids*, 32(9), 092101.

Meringolo, D.D., Liu, Y. and Lu, L., 2018. Energy analysis of wave resonance in a gap through an SPH model, *Proceedings of the Twenty-eighth International Ocean and Polar Engineering Conference*, Sapporo, Japan, ISOPE, pp. 338–344.

Miao, G.P., Saitoh, T. and Ishida, H., 2001. Water wave interaction of twin large scale caissons with a small gap between, *Coastal Engineering Journal*, 43(1), 39–58.

Molin, B., 2001. On the piston and sloshing modes in moonpools, *Journal of Fluid Mechanics*, 430, 27–50.

Ning, D.Z., Su, X.J., Zhao, M. and Teng, B., 2015. Hydrodynamic difference of rectangular-box systems with and without narrow gaps, *Journal of Engineering Mechanics*, 141(8), 04015023.

Ning, D.Z., Zhu, Y., Zhang, C.W. and Zhao, M., 2018. Experimental and numerical study on wave response at the gap between two barges of different draughts, *Applied Ocean Research*, 77, 14–25.

Perić, M. and Swan, C., 2015. An experimental study of the wave excitation in the gap between two closely spaced bodies, with implications for LNG offloading, *Applied Ocean Research*, 51, 320–330.

Saitoh, T., Miao, G.P. and Ishida, H., 2006. Theoretical analysis on appearance condition of fluid resonance in a narrow gap between two modules of very large floating structure, *Proceedings of the 3rd Asia-Pacific Workshop on Marine Hydrodynamics*, Shanghai,China, 170–175.

Song, Z.W., Lu, L., Cheng, L., Liu, Y., Tang, G.Q. and Lou, X.F., 2022. Fully nonlinear numerical investigations on the dynamics of fluid resonance between multiple bodies in close proximity, *Physics of Fluids*, 34(12), 122106.

Song, Z.W., Lu, L., Li, C., Lou, X.F., Tang, G.Q. and Liu, Y., 2021.

An effective resonant wave absorber for long regular water waves, *Applied Ocean Research*, 117, 102966.

Tan, L., Lu, L., Liu, Y., Sabodas, O.A. and Teng, B., 2014. Dissipative effects of resonant waves in confined space formed by floating box in front of vertical wall, *Proceedings of the Eleventh ISOPE Pacific/Asia Offshore Mechanics Symposium*, ISOPE, Shanghai, China.

Tan, L., Lu, L., Tang, G.Q. and Cheng, L., 2020. A dynamic solution for predicting resonant frequency of piston mode fluid oscillation in moonpools/narrow gaps, *Journal of Hydrodynamics*, 32(1), 54–69.

Vineesh, P. and Sriram, V., 2021. Numerical investigation of wave actions on two side by side boxes in close proximity using IMLPG_R method, *Applied Ocean Research*, 116, 102892.

Wang, D.G. and Zou, Z.L., 2007. Study of non-linear wave motions and wave forces on ship sections against vertical quay in a harbor, *Ocean Engineering*, 34(8–9), 1245–1256.

Wang, X.L., Qiao, D.S., Jin, L.X., Yan, J., Wang, B., Li, B.B. and Ou, J.P., 2023. Numerical investigation of wave run-up and load on heaving cylinder subjected to regular waves, *Ocean Engineering*, 268, 113415.

Wang, X.Y., Liu, Y. and Lu, L., 2022. Three-dimensional (3D) semi-analytical solution of wave-induced fluid resonance in narrow gaps of caisson-type breakwaters, *Ocean Engineering*, 253, 111305.

Yin, Y., Jiang, S.C. and Geng, B.L., 2022. Fluid resonance in the narrow gap for a box close to a bottom-mounted wall with permeable bed, *Ocean Engineering*, 258, 111726.

Zhao, W., Wolgamot, H.A., Taylor, P.H. and Eatock Taylor, R., 2017. Gap resonance and higher harmonics driven by focused transient wave groups, *Journal of Fluid Mechanics*, 812, 905–939.

Zhao, W.H., Pan, Z.Y., Lin, F., Li, B.B., Taylor, P.H. and Efthymiou, M., 2018. Estimation of gap resonance relevant to side-by-side offloading, *Ocean Engineering*, 153, 1–9.

Zhu, H.R., Zhu, R.C. and Miao, G.P., 2008. A time domain investigation on the hydrodynamic resonance phenomena of 3-D multiple floating structures, *Journal of Hydrodynamics*, *Ser. B*, 20(5), 611–616.

Zou, M.Y., Chen, M.S., Zhu, L., Li, L. and Zhao, W.H, 2023. A constant parameter time domain model for dynamic modelling of multi-body system with strong hydrodynamic interactions, *Ocean Engineering*, 268, 113376.